Phase Current Reconstruction of Open-Winding Synchronous Reluctance Motor Based on Edge-Alignment and Phase-Shift Strategy

Chong Zhang, Chun Gan, *Member, IEEE*, Kai Ni, *Member, IEEE*, Zhiyue Yu, *Student Member, IEEE*, Haochen Shi, *Member, IEEE*, and Ronghai Qu, *Fellow, IEEE*

***Abstract*—This article proposes a phase current reconstruction strategy for open-winding synchronous reluctance motor (OW-SynRM) drives with the dual-inverter topology and common dc bus. The traditional reconstruction strategy cannot be applied in OW motor drives because the dual-inverter modulation and zero-sequence current suppression strategies complicate the vector combinations and shorten their durations. Besides, additional sampling is required because the sum of the three-phase current is not zero. To solve these issues, the edge alignment algorithm is proposed to extend the duration of certain vector combinations, and the phase-shift strategy for the third sampling is proposed to obtain extra current information. In the case of the reconstruction failure in immeasurable regions, the corresponding compensation strategy is investigated. With the proposed reconstruction strategy, the system cost can be significantly reduced and the reliability can be improved, where only one current sensor is required. Besides, the single sensor can be reused for power detection and protection for the whole system by selective installation. Moreover, the proposed strategy is compatible with both the 180° and 120° assignment schemes, increasing the flexibility of application. Finally, experiments are carried out on an OW-SynRM to verify the high accuracy and feasibility of the proposed strategy.**

***Index Terms*—Dual-inverter modulation, open-winding synchronous reluctance motor (OW-SynRM), phase current reconstruction, zero-sequence current (ZSC) suppression.**

I. Introduction

SYNCHRONOUS reluctance motors (SynRMs) have attracted more and more attention due to the low manufacturing cost and high reliability. For the applications of electric vehicles and other electrified powertrains, the SynRM has been recognized as a superior candidate [1], [2]. As there is neither a permanent magnet nor winding on the rotor, the SynRM can inherently get rid of the rare-earth material demagnetization and rotor-winding heating up, so the possibility of system collapse is reduced. Additionally, the decoupled vector control scheme of an ac motor can be directly applied on the SynRM, where low current distortion and torque ripple can be ensured [3], [4]. However, to extend the application range of SynRMs, the following two requirements should be satisfied.

1) A high dc-bus voltage utilization ratio to increase the torque density of the SynRM drive system [5]–[7].
2) High system reliability and stability to prevent system collapse caused by sensor damage.

For the dc-bus voltage utilization ratio improvement, space vector pulsewidth modulation (SVPWM) has been more widely used than sinusoidal pulse width modulation. However, the three-phase two-level drive topology limits its further improvement [8]. In previous investigations [9], [10], the modular multilevel converter (MMC) topology is adopted to achieve flexible voltage selection, improve the torque capability, and achieve flexible fault tolerance in SynRM applications. Nevertheless, the MMC technology demands a more complex control scheme and a module capacitor voltage balancing solution. In [11] and [12], an approach to opening the neutral point of the stator winding is proposed so that the motor can be fed by another inverter. Benefitting from doubling the power switches, the OW topology can achieve multilevel modulation effect, higher voltage utilization, as well as better fault tolerance ability, compared with the traditional single-inverter fed topology [13]–[15]. Furthermore, the common dc-bus structure has been widely studied for saving one power supply among several power supply methods. On this occasion, zero-sequence current (ZSC) is introduced due to the existence of the zero-sequence loop, which causes extra loss and torque ripple, leading to system performance degradation.

Hence, some ZSC suppression methods have been proposed in recent years [16]–[18]. For OW-induction motor drives, the ZSC is mainly caused by the output zero-sequence voltage (ZSV) difference between two inverters. Thus, the ZSC can be eliminated by adopting an appropriate modulation scheme to counteract the ZSV difference. For an open-winding permanent magnet synchronous motor system, the third-order harmonic back electromotive force (EMF) generates extra ZSV, which is

Manuscript received June 21, 2021; revised September 25, 2021; accepted November 2, 2021. Date of publication November 16, 2021; date of current version January 19, 2022. This work was supported in part by the National Natural Science Foundation of China under Grants 52177043 and 51907073, in part by the Hubei Provincial Natural Science Foundation of China under Grant 2021CFA076, in part by the Applied Basic Frontier Program of Wuhan under Grant 2020010601012207, and in part by the Aeronautical Science Foundation of China under Grant 20200040079002. Recommended for publication by Associate Editor E. Armando. *(Corresponding author: Chun Gan.)*

The authors are with the State Key Laboratory of Advanced Electromagnetic Engineering and Technology, School of Electrical and Electronic Engineering, Huazhong University of Science and Technology, Wuhan 430074, China (e-mail: chongzhang@hust.edu.cn; chungan@hust.edu.cn; nikai@hust.edu.cn; zhiyueyu@hust.edu.cn; haochenshi@hust.edu.cn; ronghaiqu@hust.edu.cn).

Color versions of one or more figures in this article are available at https://doi.org/10.1109/TPEL.2021.3128387.

Digital Object Identifier 10.1109/TPEL.2021.3128387

the major source of ZSC in this situation [20], [21]. Besides, the inverter nonlinearity, dead time effect of switching devices, cross-coupling voltage components caused by d- and q-axis currents, and other factors will also bring in additional ZSV [22]. Among all these ZSV sources, only the ZSV output difference of the dual-inverter can be artificially controlled to eliminate the ZSC.

In terms of system stability improvement, the phase current reconstruction strategy is put forward, which employs a single current sensor to obtain the three-phase current [23]–[26]. Because only one sensor is used, the probability of system failure is decreased, where the system cost and volume can also be reduced [27]–[29]. Therefore, many schemes have been proposed in the three-phase star-connected motor system. In [30] and [31], the measurement-vector-injection-based current reconstruction strategy is proposed, which simplifies both the sampling procedures and reconstruction algorithms. As the three inserted measuring vectors synthesize an equivalent zero vector, the motor operation is not affected by the voltage vector injection. However, the PWM signals need to be rebuilt to insert the measurement vectors, where the switching loss is doubled as well. Concerning the immeasurable regions caused by the nonideal process of the bus current, the injected vectors should meet the minimum duration limit. In [32]–[34], the current reconstruction strategy with complicated wiring configurations is studied where the bus current provides useful information even when the inverter acts at the zero-vector state. However, the industrial application is limited due to complex structures. The phase-shift method-based current reconstruction strategies are proposed in [35] and [36], where no extra switching action is required. The problem of reconstruction failure in immeasurable regions is resolved by shifting the switching signals. In [37], the hybrid pulsewidth modulation (PWM) method is raised to dynamically switch PWM methods in immeasurable regions, where the current distortion is mitigated and the current reconstruction range is extended. In [38] and [39], the single current sensor is placed in one-phase branch of the motor, which has the advantage of sensing a phase current accurately. The α-axis component of stator current can be precisely obtained, whereas the β-axis component is calculated using the mathematical model. This single current sensor technology can only be used in star-connected motor drives because the precondition is that the sum of three-phase current is zero.

Nevertheless, the traditional current reconstruction strategies cannot be used in OW topologies. On the one hand, the existing phase current reconstruction strategies only focused on star-connected motor drives, where two samples of the bus current are sufficient to obtain the three-phase current. For OW motor drives, one more sample is required because the sum of three-phase current is not zero. On the other hand, the switching cycle is only divided into seven segments by the SVPWM algorithm in star-connected motor drives, where their durations are relatively long. However, the switching cycle is divided into much more segments in OW motor drives because of the dual-inverter modulation algorithm and ZSC suppression strategy. Therefore, the vector combinations are complex and their durations are short, which makes the duration of the vector combinations hard to meet the requirement of the minimum sampling time, and the sampled current is unavailable.

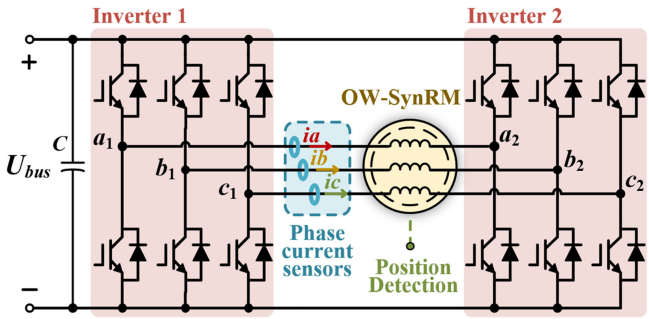

Fig. 1. Conventional OW-SynRM drive with three-phase current sensors.

This article proposes a current reconstruction strategy with ZSC detection and suppression capability for an OW-SynRM drive. To achieve this goal, the edge alignment algorithm and the phase-shift strategy for the third sampling are proposed. The edge alignment algorithm extends the duration of the active measurement vector combinations, and the phase-shift strategy for the third sampling aims to make the third sampled current available. Besides, the corresponding compensation strategies are presented in case of the reconstruction failure in the immeasurable regions. With the proposed reconstruction strategy, only one current sensor is needed in the OW system, which reduces the system cost and volume, and improves the system stability. In addition, the single sensor can be reused for the power detection of the whole system, as the installation position of the sensor is specifically selected. Moreover, the proposed strategy has a wide application range and high flexibility, because it is compatible with both 180° and 120° assignment modulation schemes.

II. Mathematical Model of an OW-SynRM Drive With ZSC Suppression

For the SynRM, low torque density is one of its major problems. As there is no winding or permanent magnet on the rotor, only the reluctance component of the electromagnetic torque is utilized, resulting in low output torque capability. Therefore, the OW topology with dual-inverter and common dc bus is adopted in this article to improve its output capability. Since the neutral point is opened and fed by another inverter, the motor input power is doubled and the low torque capability problem of SynRM can be alleviated. The conventional dual-inverter fed OW-SynRM drive topology with a common dc bus is presented in Fig. 1.

In this article, the motor inherent nonlinear factors, such as eddy currents, hysteresis losses, and the iron core saturation, have no effect on the phase current reconstruction strategy, and thus can be neglected. Hence, the voltage equations of the OW-SynRM in the $dq0$-axis synchronous rotating reference frame can be expressed as

$$\begin{bmatrix} u_d \\ u_q \\ u_0 \end{bmatrix} = \begin{bmatrix} R_s + pL_d & -\omega_e L_q & 0 \\ \omega_e L_d & R_s + pL_q & 0 \\ 0 & 0 & R_s + pL_0 \end{bmatrix} \begin{bmatrix} i_d \\ i_q \\ i_0 \end{bmatrix} \quad (1)$$

where u_d, u_q, u_0, i_d, i_q, and i_0 are the stator voltages and currents in the synchronous rotating reference frame, respectively. R_s is the stator resistance, ω_e is the electric rotor speed, and p is the differential operator. L_d, L_q, and L_0 are the $dq0$-axis self-inductances without considering the magnetic saturation. It should be noted that the zero-axis equation cannot be ignored because of the existence of the zero-sequence loop.

The electromagnetic torque can be expressed as

$$T_e = \frac{3P}{2}(L_d - L_q) i_d i_q = \frac{3P}{4}(L_d - L_q) I_s^2 \sin 2\theta \tag{2}$$

where P is the number of pole pairs, and I_s and θ are the magnitude and angle of the stator current vector, respectively. To achieve the MTPA operation, the SynRM drive usually adopts the $i_d = i_q$ control scheme.

However, severe ZSC problems will be caused by the ZSV difference between the two inverters, the inverter nonlinearity, the cross-coupling voltages component caused by dq-axis currents, and other factors [22]. The closed-loop controller should be added to suppress the ZSC, where the quasi-proportional resonant (PR) controller can be used. The quasi-PR controller achieves an abundant gain and a certain bandwidth around the selected frequency at the same time, and its typical transfer function in the s-domain can be expressed as

$$G(s) = K_p + \frac{K_r \omega_c s}{s^2 + 2\omega_c s + \omega_0^2} \tag{3}$$

where K_p and K_r are the proportional and resonant gains of the PR regulator, and ω_c and ω_0 are the cutoff and resonant frequencies, respectively. To maintain the high gain of the PR-controller at the resonant frequency, the value of ω_c should be much smaller than ω_0. And ω_0 is selected as the third-order harmonic frequency, which is the major component of ZSC.

With the quasi-PR controller, the ZSC suppression strategy is achieved. Its essence is to redistribute the duration of zero vectors (vector 0 and vector 7) of two inverters. It should be noted that the zero vectors of two inverters should be redistributed in different directions. For example, when the injected ZSV is greater than zero, Inverter 1 increases the vector 7(111) duration and Inverter 2 decreases the vector 7(111) duration. When the injected ZSV is smaller than zero, Inverter 1 decreases the vector 7(111) duration, and Inverter 2 increases the vector 7(111) duration.

III. Issues of Phase Current Reconstruction in OW-SynRM System

For the dual-inverter OW-SynRM drive, the synthetic reference voltage vector needs to be assigned to the two inverters. However, the assignment modulation can be quite flexible, as the magnitude and angle of either inverter output voltage vector can be adjusted. To balance the voltage stress of the two inverters, the output voltage vectors should have the same magnitude. In this condition, the angle is still adjustable. Fig. 2 presents the two most commonly used dual-inverter assignment modulation schemes.

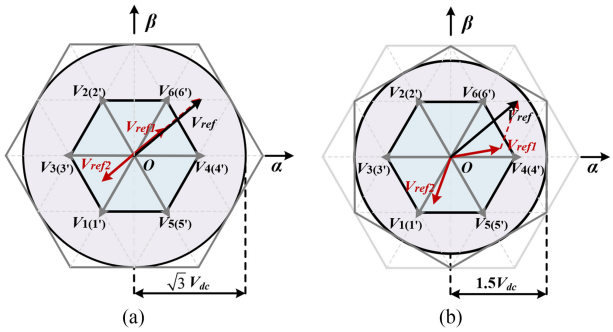

Fig. 2. Reference voltage assignment modulation strategies for dual-inverter. (a) 180° modulation scheme. (b) 120° modulation scheme.

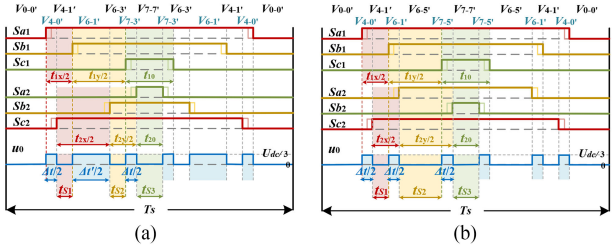

Fig. 3. Switching signals of two reference voltage assignment modulation schemes with ZSC suppression. (a) 180° assignment modulation scheme. (b) 120° assignment modulation scheme.

Both modulation schemes have both been widely used because of their different characteristics and merits. As illustrated in [22], the 180° assignment modulation scheme takes the advantage of higher voltage utilization and simpler calculation, whereas the 120° scheme takes the advantage of none undesired ZSV sources. The voltage output performance of the two schemes is widely studied, but the vector combinations and the reduction of their duration time are seldomly focused on [15]–[17]. These features are closely relevant to the success of the phase current reconstruction strategy, which will be investigated in detail in this article.

As it is known, the duration of the vectors should not be smaller than the minimum sampling time ($t_{\min}$) [23]–[25], which is about 5 μs in the physical system in this article. $t_{\min}$ is caused by many factors, such as the instantaneous oscillation of bus current, the time delay between drive signals and switch actions, the dead time of the half-bridge to avoid the simultaneous conduction of the upper and lower switches, and so on. For the OW motor drive, the dual-inverter assignment modulation scheme, as well as the ZSC suppression strategy, divide the switching period into many small segments, which results in complex vector combinations and shorter durations. The switching signals of the dual-inverter with two different assignment modulation schemes are shown in Fig. 3.

At the top of Fig. 3, $V_{\text{m-n}'}$ represents the dual-inverter state, where the output state of Inverter 1 is m and the outputs state of Inverter 2 is n. The black $V_{\text{m-n}'}$ (denoted as active vector combination, V_{ACV}) are generated because of the dual-inverter assignment modulation, and the blue $V_{\text{m-n}'}$ (denoted as zero-sequence vector combination, V_{ZSV}) are generated because of

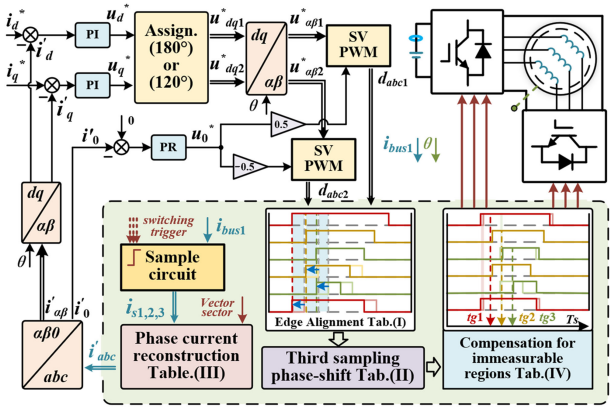

Fig. 4. Control diagram of the proposed phase current reconstruction strategy for OW-SynRM.

the ZSC suppression scheme. It can be derived by a simple calculation that the corresponding vector duration is equal for the two modulation schemes, which can be expressed as

$$\begin{cases} t_{1x} = t_{2y}, t_{1y} = t_{2x}, 180^\circ \text{ scheme} \\ t_{1x} = t_{2x}, t_{1y} = t_{2y}, 120^\circ \text{ scheme} \end{cases} \tag{4}$$

where t_{nx} is the duration of the first active vector of Inverter n, and t_{ny} is the duration of the second active vector.

It can be deduced that the duration time of V_{ACV} (t_{s1}, t_{s2}, and t_{s3}) is shortened because of the existence of V_{ZSV} duration (denoted as Δt and $\Delta t'$) in both schemes. The difference is that the duration of V_{ACV} for the 180° modulation scheme is even shorter, and $\Delta t'$ has different expressions. The value of $\Delta t'$ can be calculated as

$$\begin{aligned} \Delta t' &= \Delta t + t_{1x} - t_{2x} \\ &= \begin{cases} \Delta t + t_{1x} - t_{1y} \\ \Delta t + t_{1x} - t_{1x} \end{cases} = \begin{cases} \Delta t + t_{1x} - t_{1y}, & 180^\circ \text{ scheme} \\ \Delta t, & 120^\circ \text{ scheme}. \end{cases} \end{aligned} \tag{5}$$

Δt is determined by the output of the quasi-PR controller and it cannot be adjusted at will. Sometimes it is equal to zero during the switching cycle because of the zero-crossings of the quasi-PR controller output. Therefore, V_{ACV} instead of V_{ZSV} is chosen as the measurement vector for phase current reconstruction in the OW topology. Additionally, two more requirements need to be satisfied to measure the available current information and successfully reconstruct the three-phase currents: 1) the three times sampled values should indicate distinct current information and 2) each measurement vector should last for $t_{\min}$ at least.

IV. Proposed Phase Current Reconstruction Strategy for OW-SynRM System

The block diagram of the proposed current reconstruction strategy for the OW-SynRM drive is shown in Fig. 4. The edge alignment algorithm extends the duration of measurement vector combinations, and the third sampling strategy aims to make the third sampled current available. Besides, the compensation strategies are presented in the case of reconstruction failure in immeasurable regions. The operation principle for each part of the control diagram is described in detail in the following.

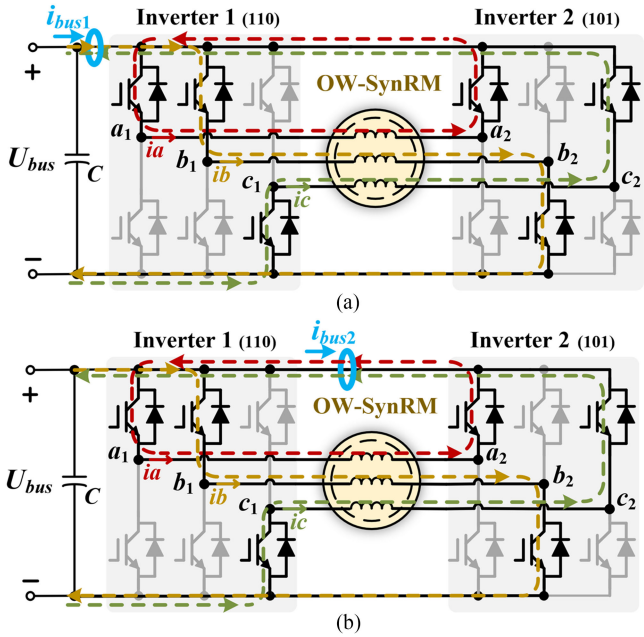

Fig. 5. Different single current sensor locations and the i_{bus} state of each while operating on the $V_{6\text{-}5'}$ state. (a) On the dc bus. (b) On the branch bus.

A. Installation Position of Single Current Sensor

To preserve the transient characteristics of the bus current, the single sensor needs to be placed behind the bus capacitors. Fig. 5 shows two typical installations of the single sensor for the OW-SynRM drives.

The assumed positive directions of the three-phase current and bus current are presented in Fig. 5. When the dual-inverter operates with the vector combination of $V_{6\text{-}5'}$, it can be seen that the measured value of i_{bus1} is $i_b - i_c$, while the measured value of the sensor between Inverters 1 and 2 is $i_a + i_c$. Despite the measured values of the two sensors are different, they both reflect the effective current information and can be used for current reconstruction. The mathematical models of bus current for the two typically installed sensors can be expressed as

$$\begin{cases} i_{\mathrm{bus1}} = (S_{abc1}^T - S_{abc2}^T) \cdot i_{abc} \\ i_{\mathrm{bus2}} = -S_{abc2}^T \cdot i_{abc} \end{cases} \tag{6}$$

where S_{abcn} is the three-phase switching state of Inverter n. i_{bus2} has a simpler expression than i_{bus1}, which is related only to the switching state of Inverter 2. Therefore, installing the single sensor on the positive dc bus between two inverters seems to be a better choice. Nevertheless, the installation position of the bus bar right behind the bus capacitor is more suitable for industrial applications. There are mainly two reasons: 1) The sensor between bus capacitor and dual-inverter can be reused for bus overcurrent protection, as it can detect the entire dc input current. 2) For the applications where voltage matching is required, it can also be reused for the internal current loop control of the former dc/dc conversion.

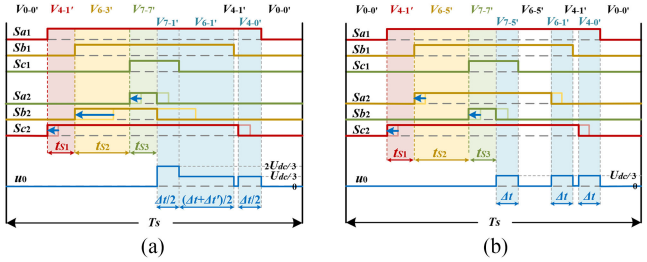

Fig. 6. Switching signals of two reference voltage assignment modulation schemes with the proposed edge alignment strategy. (a) 180° assignment modulation scheme. (b) 120° assignment modulation scheme.

Hence, the bus sensor right behind the bus capacitor with the current model i_{bus1} is selected. On this occasion, the complexity of the bus current model is significantly increased. As there are 64 vector combination states, it becomes harder to reconstruct the phase current. Therefore, a simplified model and the corresponding modulation algorithm are required.

B. Proposed Phase-Shift-Based Edge Alignment Strategy and Third-Sampling Strategy

As mentioned in Section III, both 180° and 120° assignment modulation schemes are widely used because of their particular advantages, so the proposed edge alignment strategy should be compatible with both schemes. The phase-shift method and the switching signals of each scheme are illustrated in Fig. 6. For the 180° scheme presented in Fig. 6(a), the edge alignment strategy is a little bit complicated. Since the time differences of the rising edges between relevant phases are not equal, the three-phase signals are shifted differently. The switching signal of phase A and B move forward for $\Delta t/2$, whereas the switching signal of phase C moves forward for $\Delta t'/2$. As for the 120° scheme presented in Fig. 6(b), the time differences of the rising edges between relevant phases are equal. Once the switching pulses of Inverter 2 move forward for $\Delta t/2$, the rising edges of the dual-inverter switching signals are aligned. The blue arrows indicate the phase-shift process of the edge alignment strategy.

With the proposed edge alignment strategy, the number of vector combinations is decreased and the durations of measurement vector combinations are extended. It should be noted that the rising edge alignment of the dual-inverter is not always achieved by moving the pulses of Inverter 2. When Inverter 2 is required to output more ZSV than Inverter 1, the switching duration time of Inverter 2 is longer. In this condition, the pulses of Inverter 1 move forward instead. According to the vector synthesis rule, it is clear that the total resultant vector does not change after using the edge alignment strategy. Moreover, the injected ZSV remains unchanged as well, which means the edge alignment effect on the SynRM operation is minimized. The detailed phase-shift-based rising-edge alignment strategy in each sector is summarized in Table I, where the minus sign "−" means that the corresponding pulse moves forward.

Nevertheless, the nonnegligible problem of the third sampling failure still exists. Taking the switching cycle shown in Fig. 6(a) as an example, the measurement vector combinations are $V_{4\text{-}2'}$, $V_{6\text{-}3'}$, and $V_{7\text{-}7'}$. The measured currents for $V_{4\text{-}2'}$ and $V_{6\text{-}3'}$ are available, which are $i_a - i_b$ and $i_a - i_c$. However, the measured current for $V_{7\text{-}7'}$ is zero, which does not provide useful information. Hence, the phase-shift method for the third sampling is proposed to make the third measured current available, which is briefly described as follows.

TABLE I
PHASE-SHIFT METHOD FOR EDGE ALIGNMENT STRATEGY

Voltage Sector		Sa_1	Sb_1	Sc_1	Sa_2	Sb_2	Sc_2
180° $\Delta t \geq 0$	I, IV	0	0	0	-Δt/2	-Δt′/2	-Δt/2
	II, V	0	0	0	-Δt′/2	-Δt/2	-Δt/2
	III, VI	0	0	0	-Δt/2	-Δt/2	-Δt′/2
180° $\Delta t < 0$	I, IV	-Δt/2	-Δt′/2	-Δt/2	0	0	0
	II, V	-Δt′/2	-Δt/2	-Δt/2	0	0	0
	III, VI	-Δt/2	-Δt/2	-Δt′/2	0	0	0
120° $\Delta t \geq 0$	I~VI	0	0	0	-Δt/2	-Δt/2	-Δt/2
120° $\Delta t < 0$	I~VI	-Δt/2	-Δt/2	-Δt/2	0	0	0

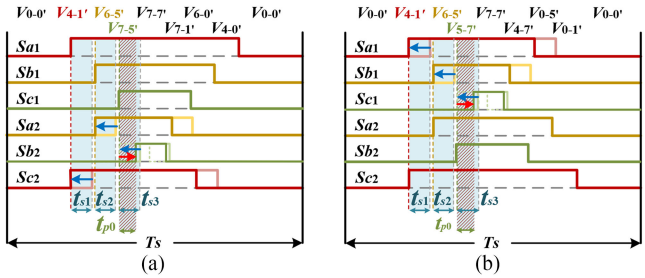

Fig. 7. Switching signals of phase-shift-based edge alignment and third sampling strategy. (a) $\Delta t \geq 0$ condition. (b) $\Delta t < 0$ condition.

Take the switching signals condition presented in Fig. 7(a) as an example, the pulse with the shortest duty cycle, which is S_{b2} of Inverter 2, moves backward. Then, the $V_{7\text{-}5'}$ with the duration t_{p0} is created, making the third measured current (i_b) available. The reason for choosing the shortest phase to move is as follows. Since the measured bus currents for the first two measurement vector combinations are available, S_{a1}, S_{b1}, S_{a2}, and S_{c2} remain unchanged for simplicity. Then, if S_{c1} is selected to move, t_{p0} might be longer than the duration of S_{b2}, which will also result in sampling failure. In consequence, S_{b2} is selected to move for the third sampling. To make it clearer, the phase-shift procedures for the third sampling in different conditions of Δt are represented by the red arrows in Fig. 7, while the phase-shift procedures of the edge alignment strategy are still represented by the blue arrows.

However, the phase that has the shortest duty cycle is determined based on several factors. To make the proposed strategy clearer, the phase-shift method for the third sampling under different modulation schemes, different voltage sectors, and different signs of Δt are summarized in Table II.

With the two phase-shift procedures represented previously, the switching signals of the dual-inverter are obtained. In each switching cycle, the adjusted switching signals produce three available $V_{\mathrm{m\text{-}n'}}$ that last long enough, then three different current information is obtained. Furthermore, the rising edge alignment method reduces the number of available $V_{\mathrm{m\text{-}n'}}$ from 36 (6×6)

TABLE II
PHASE-SHIFT METHOD FOR THIRD SAMPLING STRATEGY

Voltage Sector		Phase Selected for Third Sampling
180° scheme	I	Sa_2 for $\Delta t \geq 0$, Sc_1 for $\Delta t < 0$
	II	Sb_2 for $\Delta t \geq 0$, Sc_1 for $\Delta t < 0$
	III	Sb_2 for $\Delta t \geq 0$, Sa_1 for $\Delta t < 0$
	IV	Sc_2 for $\Delta t \geq 0$, Sa_1 for $\Delta t < 0$
	V	Sc_2 for $\Delta t \geq 0$, Sb_1 for $\Delta t < 0$
	VI	Sa_2 for $\Delta t \geq 0$, Sb_1 for $\Delta t < 0$
120° scheme	I, II	Sb_2 for $\Delta t \geq 0$, Sc_1 for $\Delta t < 0$
	III, IV	Sc_2 for $\Delta t \geq 0$, Sa_1 for $\Delta t < 0$
	V, VI	Sa_2 for $\Delta t \geq 0$, Sb_1 for $\Delta t < 0$

TABLE III
RELATIONSHIP BETWEEN THE MEASURED BUS CURRENT AND THE VECTOR COMBINATION OF DUAL-INVERTER

$V_{\text{m-n'}}$	i_{bus1}	$V_{\text{m-n'}}$	i_{bus1}
$V_{1\text{-}2'}$	$i_c - i_b$	$V_{7\text{-}3'}$	i_a
$V_{2\text{-}4'}$	$i_b - i_a$	$V_{7\text{-}5'}$	i_b
$V_{3\text{-}6'}$	$i_c - i_a$	$V_{7\text{-}6'}$	i_c
$V_{4\text{-}1'}$	$i_a - i_c$	$V_{3\text{-}7'}$	$-i_a$
$V_{5\text{-}3'}$	$i_a - i_b$	$V_{5\text{-}7'}$	$-i_b$
$V_{6\text{-}5'}$	$i_b - i_c$	$V_{6\text{-}7'}$	$-i_c$

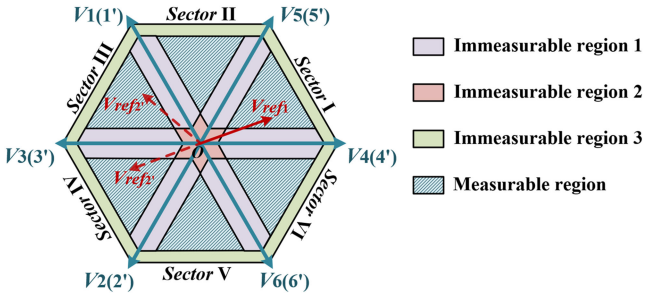

Fig. 8. Immeasurable regions of the OW-SynRM system.

to 6. In addition, the phase-shift-based third sampling strategy generates several other $V_{\text{m-n}'}$, where one inverter adopts V_7, and the other inverter adopts V_3, V_5, or V_6. In general, the relationships between the measured current and the vector combination of the dual-inverter are represented in Table III.

As shown in Table III, there are two $V_{\text{m-n}'}$ in the left table and one $V_{\text{m-n}'}$ in the right table in every switching cycle, where the bus current in each $V_{\text{m-n}'}$ is measured. Based on these three sampled currents, the three-phase current can be effectively reconstructed in the SynRM drive.

C. Compensation Strategy in Immeasurable Regions

Although the rising edge alignment strategy increases the duration of V_{ACV}, there still exist immeasurable regions, where the requirement of $t_{\min}$ is not met [23]–[25]. These immeasurable regions are shown in Fig. 8, where two regions are similar to that of the star-connected motor and one region is different. Moreover, it can be deduced from (4) and Fig. 8 that V_{ref1} and V_{ref2} will enter the immeasurable region at the same time, regardless of whichever assignment modulation scheme is adopted. Therefore, V_{ref1} is substituted for the corresponding synthesized voltage vector to simplify the description.

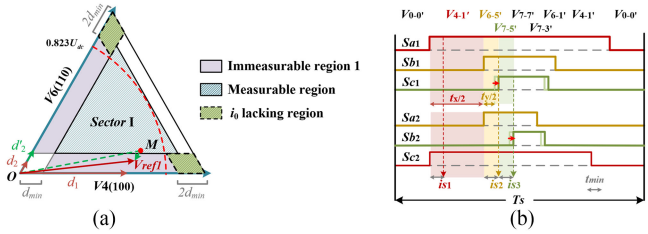

Fig. 9. Compensation method of the immeasurable region 1. (a) Adjusted synthesis vector of V_{ref1} diagram. (b) Modulated switching signals.

When the duration time of one V_{ACV} is smaller than $t_{\min}$, the corresponding current sampling is not available. This condition is presented in Fig. 8 as immeasurable region 1 (in purple). When both the two V_{ACV} do not last long enough, the system will operate in immeasurable region 2 (in red), where the samplings in both two active voltage vectors are not available. Moreover, an additional one is added inevitably (in green), which is caused by the lack of duration of the $V_{\text{m-n}'}$ for the third sampling.

The compensation methods of each region are analyzed and summarized as follows.

As shown in Fig. 8, the immeasurable regions are divided into six parts according to sectors, but the compensation strategies are similar. Therefore, the compensation strategy of immeasurable regions in Sector I is taken as an example for detailed analysis and deduction, and the compensation strategy in other sectors can be deduced in the same way.

1) *Immeasurable region 1:* In this region, one of the first two $V_{\text{m-n}'}$ durations is sufficient and the other one is deficient, where the judgment equation can be expressed as

$$\max\{t_{1x}/2, t_{1y}/2\} \geq t_{\min},\ \min\{t_{1x}/2, t_{1y}/2\} < t_{\min}. \quad (7)$$

The situations of $t_{1x} \geq t_{1y}$ and $t_{1x} < t_{1y}$ can be considered symmetric about the angular bisectors of Sector I, so the compensation algorithms in both situations are similar. Taking the $t_{1x} \geq t_{1y}$ situation as an example, the vector falls in the immeasurable region 1, as shown in Fig. 9(a). The red arrows represent the phase-shift procedure of the compensation method in Fig. 9(b).

As shown in Fig. 9, the duration time of $V_{4\text{-}1'}$ (d_1) meets the requirement of $d_{\min}$ ($t_{\min}$ / t_s), while $V_{6\text{-}5'}$ (d_2) does not. To extend the duration of V_6 from d_2 to d'_2, the pulses of S_{c1} and S_{b2} are shifted backward for

$$\Delta t_{c1} = \Delta t_{b2} = t_{\min} - t_y/2. \quad (8)$$

Additionally, the duration of the third $V_{\text{m-n}'}$ needs to be long enough, which means that the falling edge of the phase with the second shortest duty cycle [S_{c1} or S_{a2} in Fig. 9(b)] cannot precede the rising edge of S_{b2}, which can be calculated as

$$\begin{cases} t_{c1} = t_0 + \Delta t \\ t_{a2} = t_0 + t_y \\ t_{b2} = t_0 \end{cases} \quad (9)$$

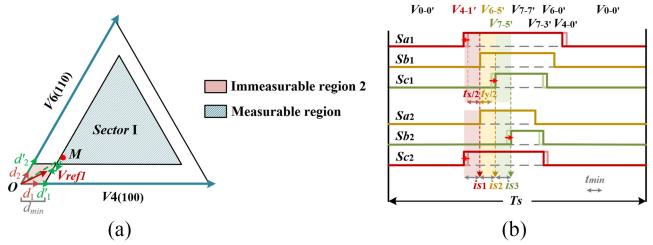

Fig. 10. Compensation method of the immeasurable region 2. (a) Adjusted synthesis vector of V_{ref1} diagram. (b) Modulated switching signals.

where t_0 is the duration of the injected zero vector (111) of both inverters, and the following relationship should be satisfied:

$$\begin{cases} t_{c1} \geq t_{p0} = t_{\min} \\ t_{a2} \geq t_y/2 + \Delta t_{c1} + t_{p0}. \end{cases} \tag{10}$$

Simplifying (8), (9), and (10), the following relationship can be obtained as:

$$\begin{cases} t_0 + \Delta t \geq t_{\min} \\ t_0 + t_y \geq 2t_{\min}. \end{cases} \tag{11}$$

As the minimum values of Δt and t_y are 0, t_0 should not be shorter than $2t_{\min}$, which is 10 μs.

2) *Immeasurable region 2:* In this region, the durations of the first two $V_{\text{m-n}'}$ are both deficient, which can be expressed as

$$\max\{t_{1x}, t_{1y}\} < t_{\min}. \tag{12}$$

Fig. 10 shows the compensation method in immeasurable region 2. In the low modulation region shown in Fig. 10(a), d_1 and d_2 need to be increased to d'_1 and d'_2, respectively. The adjustment process is shown in Fig. 10(b), where the red arrows represent the phase-shift procedure.

To increase d_1 and d_2, the switching pulses of S_{a1} and S_{c2} are shifted forward, and the switching pulses of S_{c1} and S_{b2} are shifted backward. Each phase-shift value can be calculated as

$$\begin{cases} \Delta t_{a1} = \Delta t_{c2} = t_{\min} - t_x/2 \\ \Delta t_{c1} = \Delta t_{b2} = t_{\min} - t_y/2. \end{cases} \tag{13}$$

Under the assumption of $t_0 = 10$ μs, the conditions in (9) are satisfied. Furthermore, the falling edge of S_{c2} should also be taken into consideration

$$\begin{aligned} t_{c2} &= t_0 + t_x + t_y \geq t_x/2 \\ &\quad + \Delta t_{c2} + t_y/2 + \Delta t_{c1} + t_{p0} = 3t_{\min}. \end{aligned} \tag{14}$$

Since t_x and t_y can be close to 0, t_0 should be larger than $3t_{\min}$ in the immeasurable region 2. However, the duration of zero vector in this situation is long enough to be redistributed, which does not affect the maximum linear modulation range. Table IV represents the selected phase-shift signals for the compensation strategies in all sectors.

For the immeasurable region 3, as shown in Fig 8, the motor operates in the high modulation region, which is close to the boundary of the linear modulation area. In this situation, the active vectors take up the dominant part of the switching cycle, leaving no extra duration for the third sampling. Therefore, the duration of the third $V_{\text{m-n}'}$ is always deficient in this region, which results in a 5% reduction in the linear modulation area (10 kHz switching frequency, 5 μs reserved for the third $V_{\text{m-n}'}$).

TABLE IV
PHASES SELECTED FOR COMPENSATION STRATEGIES IN IMMEASURABLE REGIONS

Voltage Sector	Immeasurable region 1 $t_0 = 2t_{min}$	Immeasurable region 2 $t_0 = 3t_{min}$
I	*if* $(t_x/2 < t_{min})$ Sa_1, Sc_2 || *if* $(t_y/2 < t_{min})$ Sc_1, Sb_2	
II	*if* $(t_x/2 < t_{min})$ Sb_1, Sa_2 || *if* $(t_y/2 < t_{min})$ Sc_1, Sb_2	
III	*if* $(t_x/2 < t_{min})$ Sb_1, Sa_2 || *if* $(t_y/2 < t_{min})$ Sa_1, Sc_2	
IV	*if* $(t_x/2 < t_{min})$ Sc_1, Sb_2 || *if* $(t_y/2 < t_{min})$ Sa_1, Sc_2	
V	*if* $(t_x/2 < t_{min})$ Sc_1, Sb_2 || *if* $(t_y/2 < t_{min})$ Sb_1, Sa_2	
VI	*if* $(t_x/2 < t_{min})$ Sa_1, Sc_2 || *if* $(t_y/2 < t_{min})$ Sb_1, Sa_2	

In general, the algorithm in the immeasurable region 2 realizes the compensation perfectly, whereas the algorithm in the immeasurable region 1 needs to satisfy the condition of $t_0 = 2t_{\min}$ (10 μs). However, the decline in voltage utilization does not worsen. As shown in Fig. 9(a), the maximum linear modulation index can be calculated as

$$M = \frac{\sqrt{3}/2U_{\text{dc}} \times (1 - 0.5)}{U_{\text{dc}}} = 0.823. \tag{15}$$

Equation 15 means that the i_0 lacking region [$0.9U_{\text{dc}}$, as shown in Fig. 9(a)] falls outside the linear modulation region, thus having no effect on the linear modulation range of the system. In a word, despite the immeasurable region 3 cannot be eliminated, the voltage utilization of the system is only reduced by 5%.

D. Discussion and Comparison

For further industrial application, the compatibility of the proposed current reconstruction strategy on encoderless control is discussed in the following. The rotor position estimation algorithm of SynRM can be divided into two kinds of methods. One is based on the mathematical model of the motor, which mainly uses the EMF to estimate the rotor position and velocity [40]–[42], where only the voltage and current information is required. As the proposed current reconstruction strategy provides the precise three-phase current, it is compatible with this kind of encoderless method. The other kind of encoderless control is based on the salient effect of the rotor, where the high-frequency (HF) signal injection strategies are utilized. To inject the HF signals, the voltage reference value needs to be modulated. This will make it difficult to eliminate the immeasurable regions when using the proposed current reconstruction strategy. Thus, the proposed reconstruction strategy is not suitable for this kind of encoderless technology.

Besides, the comparison between the proposed system and the existing methods is carried out in Table V. The existing current reconstruction strategies can be divided into three kinds: the measurement pulse injection methods [30], [31], the wiring reconfiguration methods [32]–[34], and the phase-shift-based method [35], [36]. What they have in common is that they are proposed for the star-connected motor drives, where just one current sensor is saved. Only the proposed method can be applied to the OW topology, where two current sensors are saved.

TABLE V
COMPARISON OF THE PROPOSED AND EXISTING CURRENT RECONSTRUCTION STRATEGY

Item \ Method	Method in [30]-[31]	Method in [32]-[34]	Method in [35]-[36]	Proposed method
Suitable for OW topology	No	No	No	Yes
Reduction of sensor number	One	One	One	Two
Wiring reconfiguration	Not required	Required	Not Required	Not required
Additional injected pulse	Required	Not required	Not Required	Not required
Complexity	Low	Medium	Medium	High

TABLE VI
MAIN PARAMETERS OF THE MOTOR AND CONTROL SYSTEM

Parameters	Unit	Value
Pole number	-	4
Stator slot number	-	24
Rotor internal layers	-	3
Rated power	W	300
Rated speed	r/min	1500
Maximum phase inductance	μH	76
Minimum phase inductance	μH	43
Stator resistance	mΩ	3.1
Air gap	mm	0.3
Sampling & Controlling frequency	kHz	10
t_{min}	μs	5
Switching dead time	μs	2

Besides, additional measurement pulses injection is needed in the methods proposed in [30] and [31], which results in extra switching losses. Wiring reconfiguration is needed in [32]–[34], which will complicate the circuit wiring and increase the system volume. Nevertheless, the proposed method is the most complex in terms of the reconstruction algorithm because of the edge alignment and third sampling procedures.

V. EXPERIMENTAL VERIFICATION

To verify the proposed phase current reconstruction strategy, experiments are carried out on a three-phase OW-SynRM driven by a dual-inverter topology with a common dc bus. The main parameters of the system are listed in Table VI. The experimental platform is shown in Fig. 11(a), and the schematic diagram of the motor drive is illustrated in Fig. 11(b). The dual-inverter consists of six IGBT half-bridge modules, and is powered by a programmable voltage source where the dc voltage output is set as 80 V. The sampling and switching frequencies are both 10 kHz. The dc-bus current and three-phase currents are sampled by Hall-effect current sensors LA55P/SP1 and the rotor position is detected by a resolver. The digital control system is designed based on a TMS320F28377D platform. The experimental waveforms are recorded by a multichannel isolated oscilloscope. The load torque is provided by a magnetic brake. A torque sensor and a gearbox are installed between the motor and the load, to measure and amplify the torque, respectively. Specifically, the single sensor is installed between the bus capacitor and the dual-inverter.

Fig. 12 shows the experimental results of the bus current and the switching states during one switching cycle under 180° assignment modulation with and without the proposed phase-shift

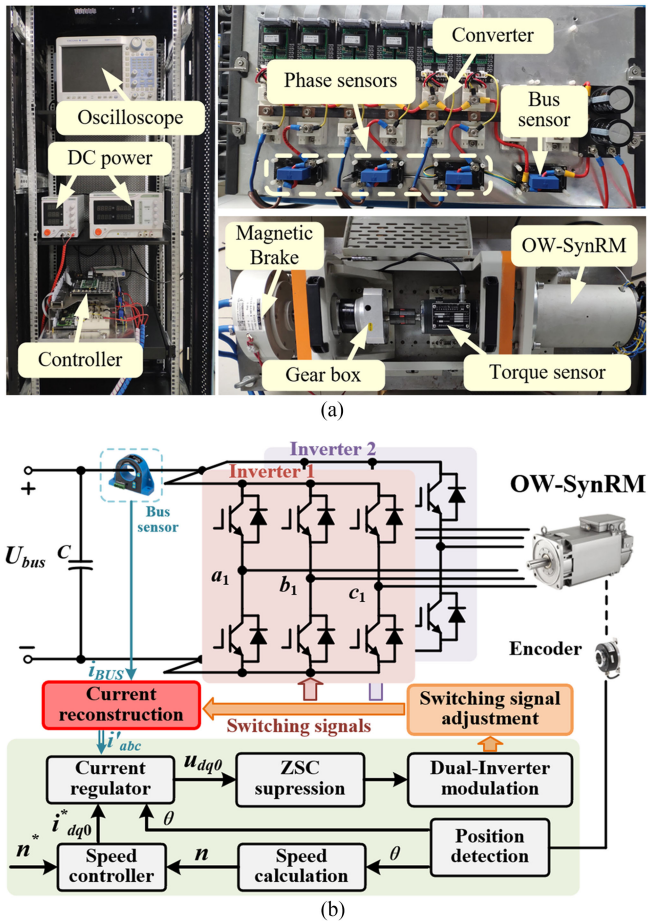

Fig. 11. Experimental setup for the overall system. (a) Photograph of the test platform. (b) Schematic diagram.

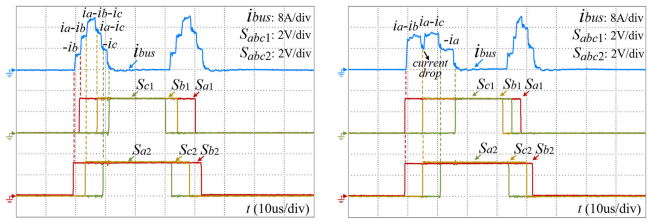

Fig. 12. Experimental results of the bus current and switching states with 180° assignment modulation scheme when $\Delta t < 0$. (a) Without the proposed scheme. (b) With the proposed scheme.

strategy. In the figure, $i_{\rm bus}$ is the detected bus current, and S_{abc1}, S_{abc2} are the switching signals of dual-inverter, respectively. As shown in Fig. 12(a), the switching signal is centrally symmetric about the switching period without the proposed strategies. Hence, only the first half cycle is considered. It can be seen that the bus current has five nonzero states in the first half cycle, which are related to the switching states. Although these current states contain redundant information about the three-phase current, the duration of each state is too short for accurate current sampling, resulting in reconstruction failure. When the proposed phase-shift method (180° scheme in Tables I and II) and compensation strategy (see Table IV) are applied, the five

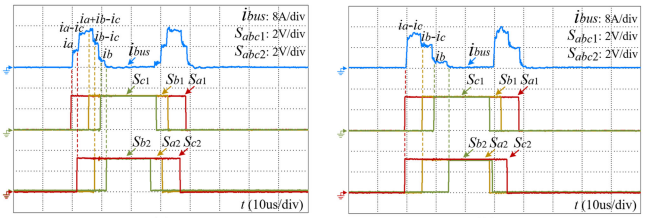

Fig. 13. Experimental results of the bus current and switching states with 120° assignment modulation scheme when $\Delta t > 0$. (a) Without the proposed scheme. (b) With the proposed scheme.

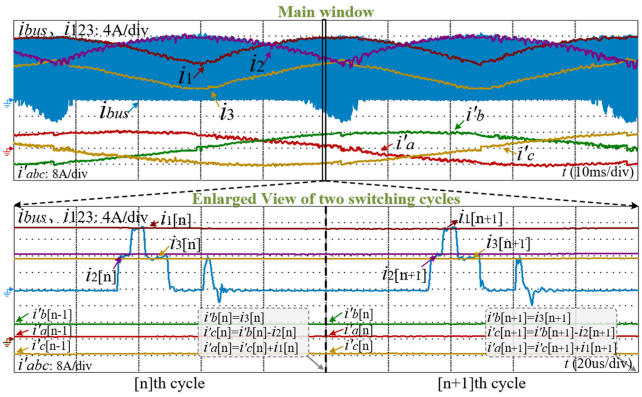

Fig. 14. Experimental results of the sampling current i_{123} and the reconstructed three-phase current i'_{abc} in the main window and enlarged view at 200 r/min.

current states in Fig. 12(a) are merged into two nonzero states and an additional current state. In Fig. 12(b), the bus current states are significantly simplified, and the different current states, $i_a - i_b$, $i_a - i_c$, $-i_a$ last long enough to be measured accurately.

In Fig. 12(b), there exists a small current drop between the first two current states, which lasts for about 2 μs. This is caused by the dead time of upper and lower switches, where additional current states are presented. Taking the switching state in Fig. 12(b) as an example, the actual output voltages of b_1 and c_2 in Fig. 1 are uncontrollable during the dead time, which are determined by the current polarities of i_b and i_c, respectively. The lower antiparallel diode of b_1 conducts when $i_b > 0$ and the upper diode conducts when $i_b < 0$. The same principle applies to the diodes of c_2 as well. Therefore, there are 4 (2×2) possible output voltage scenarios in the dead time near the aligned rising edge of switching signals. Among them, the current state of i_a-i_b remains only when $i_b > 0$ and $i_c > 0$; otherwise, a small current drop or rise will occur. As the dead-time effect has already been considered when evaluating $t_{\min}$, the effective measurement of i_a-i_b has been completed before the current drop and the dead-time effect will not affect accurate current sampling.

Fig. 13 shows the experimental results of the bus current and the switching states during one switching cycle under 120° assignment modulation with and without the proposed phase-shift strategy. The bus current still has five nonzero states in the first half cycle, where the duration time of each state is too short for accurate sampling. The edge alignment scheme and the phase-shift method for the third sampling in this condition are slightly different, where S_{a2}, S_{b2}, and S_{c2} are shifted forward for $\Delta t/2$, and S_{b2} is selected to be shifted for the third sampling (120° scheme in Tables I and II).

It can be seen from Figs. 12 and 13 that the bus current in the second half switching cycle becomes different from that of the first half one after adopting the proposed scheme, which indicates extra current information. However, the actual $V_{\text{m-n}'}$ states in the second half cycle are not clear and their durations are passively determined by the proposed scheme, which cannot be changed according to the requirement. Therefore, the second half cycle cannot be used for effective sampling.

In Fig. 14, the experimental results of the bus current i_{bus} and the sampling currents i_1, i_2, and i_3 at 200 r/min are presented, and the principle of the phase current reconstruction control strategy is particularly represented in the enlarged view of two adjacent cycles. As shown in the figure, i_1 and i_2 alternate with each other and form the upper envelope curve of i_{bus}, and i_3 intersects with the sampled i_1, i_2, and i_3 with the reconstruction strategy listed in Table III, which is presented in the enlarged view.

Suppose that the two amplified periods are the [n]th and [n+1]th cycles, the calculation process is as follows. First, the i_1[n−1], i_2[n−1], and i_3[n−1] sampled in the [n−1]th cycle are utilized for calculating the reconstructed three-phase current i'_a[n−1], i'_b[n−1], and i'_c[n−1]. Second, the reconstructed currents are used in the control system to generate the switching signals for the [n]th cycle. Third, the switches of the dual-inverter act accordingly to control the three-phase current, and i_{bus} in the [n]th cycle is recorded as i_1[n], i_2[n], and i_3[n] when each measurement vector is adopted, respectively. Then, the calculation and control strategy can be extended to the [n+1]th cycle in the same manner.

It should be noted that the enlarged view of two adjacent switching cycles is selected where the synthetic reference voltage vector is situated in Sector I. In this situation, the sampled i_1 equals to $i_a - i_c$ when the dual-inverter is in the $V_{4\text{-}1'}$ state; the sampled i_2 equals to $i_b - i_c$ when the dual-inverter is in the $V_{6\text{-}5'}$ state; and the sampled i_3 equals to i_b when the dual-inverter is in the $V_{7\text{-}5'}$ state. When the synthetic reference voltage vector locates in other sectors, the sampled i_1, i_2, and i_3 reflect different current information, and the corresponding reconstruction calculation equations are adopted.

The experimental results of the actual and reconstructed three-phase current (i_{abc} and i'_{abc}) with and without the PR-based ZSC suppression strategy are shown in Fig. 15, where the ZSC suppression strategy is employed at the middle point of the curve. The magnitude of each harmonic component and the total harmonic distortion (THD) of i_a can be derived using the Fast Fourier transform algorithm. Without the PR-based ZSC suppression scheme, the magnitude of the third-order harmonic current is 20.4%, which makes up the dominant component that causes the current distortion, and the THD is 21.39%. With the ZSC suppression strategy, the magnitude of the third-order harmonic current is well eliminated to only 1.16%, where the THD is reduced to only 5.16%. However, the proposed three-times-sampling strategy is still needed to detect i_0 for the ZSC suppression. The point to be emphasized here is that the proposed reconstruction strategy can be achieved regardless of

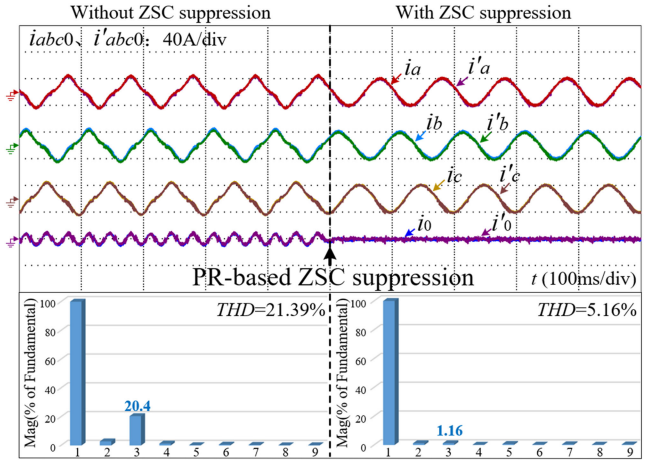

Fig. 15. Experimental results of the reconstructed three-phase current i'_{abc} with and without ZSC suppression strategy.

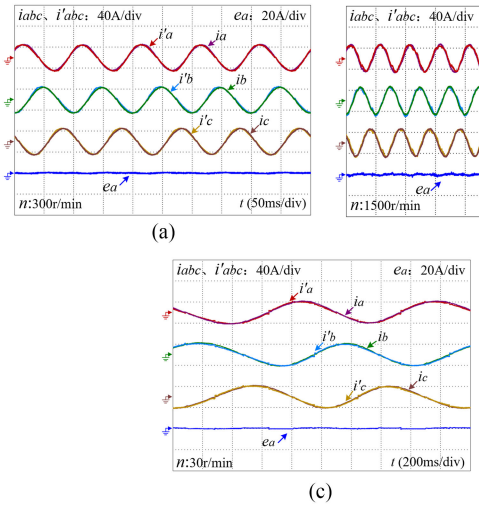

Fig. 16. Experimental results of the comparison between the actual three-phase current (i_{abc}) and reconstructed three-phase current (i'_{abc}) and the reconstruction error of phase A (e_a) under no-load condition. (a) 300 r/min. (b) 1500 r/min. (c) 30 r/min.

whether the phase current contains the ZSC component, which is the most prominent difference compared with traditional current reconstruction strategies.

Experiments are carried out at 300, 1500 r/min, and the extremely low 30 r/min under no-load conditions to verify the effectiveness of the proposed current reconstruction scheme. Experimental results of i_{abc}, i'_{abc}, and e_a are illustrated in Fig. 16, where e_a is the reconstruction error of phase A. It can be seen that i_{abc} matches well with i'_{abc}, which verifies the effectiveness of the proposed reconstruction strategy over a wide range of speeds. In Fig. 16(a), the amplitudes of the actual current i_a and reconstruction error e_a are 26.6 A and 0.8 A, respectively, where the relative reconstruction error is 3.0%. As the speed increases in Fig. 16(b), those two amplitudes rise to 27.2 A and 1.3 A, where the relative reconstruction error is 4.8%. Despite the reconstruction effect decreases slightly with the increase of rotor speed, the error is still low enough for

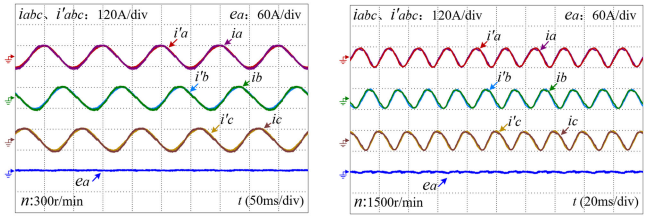

Fig. 17. Experimental results of the comparison of the actual three-phase current (i_{abc}) and reconstructed three-phase current (i'_{abc}) and the reconstruction error of phase A (e_a) with 2 N·m load. (a) 300 r/min. (b) 1500 r/min.

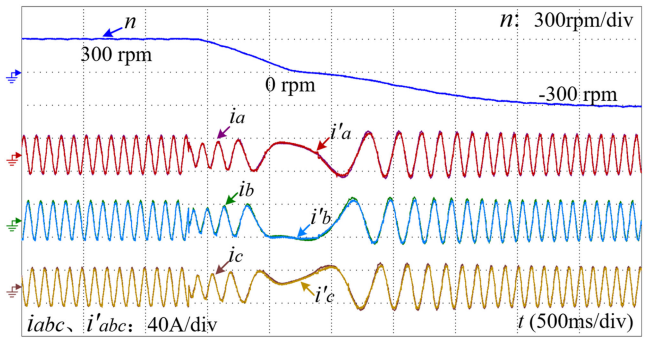

Fig. 18. Experimental results of the comparison between the actual three-phase current (i_{abc}) and reconstructed three-phase current (i'_{abc}) in reversing process.

motor control. Even in the extremely low-speed condition, as shown in Fig. 16(c), the relative error is only 3.6%, ensuring high accuracy.

Experiments are also carried out at 300 r/min and 1500 r/min under 2 N·m load condition, as shown in Fig. 17. The amplitudes of i_a and e_a are 56.8 A and 1.6 A at 300 r/min, where the relative reconstruction error is 2.8%. Comparing with the no-load condition in Fig. 16(a), the relative error is slightly decreased with the increase of the load torque. This is due to the rapid increase of the three-phase current amplitude. A similar phenomenon exists in the 1500 r/min condition, where the amplitudes of i_a and e_a are 58.2 and 2.8 A, and the relative reconstruction error is 4.8%.

To verify the dynamic performance of the proposed strategy, the experiment of a large speed step is carried out. Fig. 18 shows the results of the system performance in the reversing process from 300 to −300 r/min, where n is the actual speed. As can be seen from Fig. 18, it takes about 0.75 s for the motor to decelerate from 300 r/min to 0, and about 2 s to reversely accelerate to −300 r/min. As can be seen in Fig. 18, the reconstructed three-phase current tracks the actual ones well during the whole speed regulating process.

The experiment is also carried out to further verify the dynamic characteristics of the proposed reconstruction strategy under the torque mutation conditions. In Fig. 19, the blue curve represents the electromagnetic torque T_e. Due to the friction on the rotating shaft, the load torque is about 0.5 N·m at the beginning. Then, the load torque is increased to 1 N·m, where the dynamic settling time is about 0.25 s. Afterward, the load torque is increased to 2 N·m, which takes about 0.3 s. Finally,

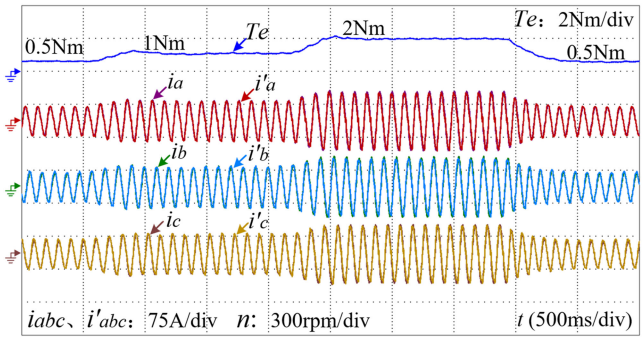

Fig. 19. Experimental results of the comparison between the actual three-phase current (i_{abc}) and the reconstructed three-phase current (i'_{abc}) under the torque mutation condition.

the load torque falls back to 0.5 N·m, where the settling time is about 0.45 s. It can be seen from the figure that the reconstructed three-phase current tracks well with the actual ones in the whole torque mutation process.

In general, the effectiveness of the proposed current reconstruction strategy for OW-SynRM is proved in a wide range of speed and torque. In addition, with the proposed phase-shift scheme, the current reconstruction strategy is feasible regardless of whether the 180° or 120° assignment modulation scheme is adopted in the dual-inverter topology. Besides, the three-phase current can be precisely reconstructed regardless of whether the phase current contains the ZSC component. Therefore, the proposed current reconstruction scheme is proved to have high compatibility.

VI. Conclusion

This article proposes a new phase current reconstruction strategy for the OW-SynRM drive, where the ZSC component of the three-phase current can be detected. The traditional current reconstruction strategy cannot be directly applied to the OW drive topology, as the dual-inverter assignment scheme and ZSC suppression strategy divide the switching cycle into segments with shorter durations. The proposed phase-shift-based edge alignment algorithm decreases the number of total vector combinations and extends the durations of the active measurement vector combinations, with which two effective current information can be obtained in each switching cycle. Besides, the phase-shift strategy for the third sampling is developed to obtain additional current information. Furthermore, the compensation strategy is investigated in the case of reconstruction failure in immeasurable regions. Finally, the high feasibility and accuracy of the proposed reconstruction strategy are verified by experiments. The major contributions and advantages can be summarized as follows.

1) Only one current sensor is used in OW-SynRM system, reducing the system cost and volume, which can also provide a fault-tolerant alternative for phase current sensors in highly reliable applications.
2) The dc-bus current sensor can be reused for total power detection for the whole system by specifically selecting the installation position.
3) Whether the ZSC is suppressed or not, the three-phase current can be reconstructed independently.
4) The proposed strategy is compatible with both 180° and 120° assignment modulation schemes, increasing the application flexibility.
5) The proposed scheme is convenient for wire connection, and the commercial six-switch modules can be utilized, which is beneficial for industrial applications.

References

[1] M. N. Ibrahim, P. Sergeant, and E. M. Rashad, "Relevance of including saturation and position dependence in the inductances for accurate dynamic modeling and control of SynRMs," *IEEE Trans. Ind. Appl.*, vol. 53, no. 1, pp. 151–160, Jan./Feb. 2017.

[2] M. N. Ibrahim, P. Sergeant, and E. M. Rashad, "Synchronous reluctance motors performance based on different electrical steel grades," *IEEE Trans. Magn.*, vol. 51, no. 11, Nov. 2015, Art. no. 7403304.

[3] S. Taghavi and P. Pillay, "A novel grain-oriented lamination rotor core assembly for a synchronous reluctance traction motor with a reduced torque ripple algorithm," *IEEE Trans. Ind. Appl.,* vol. 52, no. 5, pp. 3729–3738, Sep./Oct. 2016.

[4] A. Arafat and S. Choi, "Torque ripple minimization of a five-phase permanent magnet assisted synchronous reluctance motor at open-phase faults," in *Proc. IEEE Appl. Power Electron. Conf. Expo.*, 2017, pp. 1–6.

[5] M. N. F. Ibrahim, A. S. Abdel-Khalik, E. M. Rashad, and P. Sergeant, "An improved torque density synchronous reluctance machine with a combined star-delta winding layout," *IEEE Trans. Energy Convers.*, vol. 33, no. 3, pp. 1015–1024, Sep. 2018.

[6] C. Mademlis, "Compensation of magnetic saturation in maximum torque to current vector controlled synchronous reluctance motor drives," *IEEE Trans. Energy Convers.*, vol. 18, no. 3, pp. 379–385, Sep. 2003.

[7] M. N. Ibrahim, P. Sergeant, and E. M. Rashad, "Combined star-delta windings to improve synchronous reluctance motor performance," *IEEE Trans. Energy Convers.*, vol. 31, no. 4, pp. 1479–1487, Dec. 2016.

[8] S. Mukherjee, S. K. Giri, and S. Banerjee, "A flexible discontinuous modulation scheme with hybrid capacitor voltage balancing strategy for three-level NPC traction inverter," *IEEE Trans. Ind. Electron.*, vol. 66, no. 5, pp. 3333–3343, May 2019.

[9] C. Gan, Q. Sun, J. Wu, W. Kong, C. Shi, and Y. Hu, "MMC-based SRM drives with decentralized battery energy storage system for hybrid electric vehicles," *IEEE Trans. Power Electron.*, vol. 34, no. 3, pp. 2608–2621, Mar. 2019.

[10] C. Gan, J. Wu, Y. Hu, S. Yang, W. Cao, and J. M. Guerrero, "New integrated multilevel converter for switched reluctance motor drives in plug-in hybrid electric vehicles with flexible energy conversion," *IEEE Trans. Power Electron.*, vol. 32, no. 5, pp. 3754–3766, May 2017.

[11] Z. Yu, C. Gan, Y. Chen, and R. Qu, "DC-biased sinusoidal current excited switched reluctance motor drives based on flux modulation principle," *IEEE Trans. Power Electron.*, vol. 35, no. 10, pp. 10614–10628, Oct. 2020.

[12] D. Casadei, G. Grandi, A. Lega, and C. Rossi, "Multilevel operation and input power balancing for a dual two-level inverter with insulated DC sources," *IEEE Trans. Ind. Appl.*, vol. 44, no. 6, pp. 1815–1824, Nov./Dec. 2008.

[13] W. Zhao, P. Zhao, D. Xu, Z. Chen, and J. Zhu, "Hybrid modulation fault tolerant control of open-end windings linear vernier permanent-magnet motor with floating capacitor inverter," *IEEE Trans. Power Electron.*, vol. 34, no. 3, pp. 2563–2572, Mar. 2019.

[14] H. Zhan, Z. Zhu, and M. Odavic, "Analysis and suppression of zero sequence circulating current in open winding PMSM drives with common DC bus," *IEEE Trans. Ind. Appl.*, vol. 53, no. 4, pp. 3609–3620, Jul./Aug. 2017.

[15] Y. Zuo, X. Zhu, X. Si, and C. H. T. Lee, "Fault-tolerant control for multiple open-leg faults in open-end winding permanent magnet synchronous motor system based on winding reconnection," *IEEE Trans. Power Electron.*, vol. 36, no. 5, pp. 6068–6078, May 2021.

[16] A. Edpuganti and A. K. Rathore, "New optimal pulsewidth modulation for single DC-link dual-inverter fed open-end stator winding induction motor drive," *IEEE Trans. Power Electron.*, vol. 30, no. 8, pp. 4386–4393, Aug. 2015.

[17] S. Jain, R. Karampuri, and V. T. Somasekhar, "An integrated control algorithm for a single-stage PV pumping system using an open-end winding

induction motor," *IEEE Trans. Ind. Electron.*, vol. 63, no. 2, pp. 956–965, Feb. 2016.
[18] Q. An, J. Liu, Z. Peng, L. Sun, and L. Sun, "Dual-space vector control of open-end winding permanent magnet synchronous motor drive fed by dual inverter," *IEEE Trans. Power Electron.*, vol. 31, no. 12, pp. 8329–8342, Dec. 2016.
[19] V. T. Somasekhar, S. Srinivas, and K. K. Kumar, "Effect of zero-vector placement in a dual-inverter fed open-end winding induction motor drive with alternate sub-hexagonal center PWM switching scheme," *IEEE Trans. Power Electron.*, vol. 23, no. 3, pp. 1584–1591, May 2008.
[20] Y. Zhou and H. Nian, "Zero-sequence current suppression strategy of open winding PMSG system with common DC bus based on zero vector redistribution," *IEEE Trans. Ind. Electron.*, vol. 62, no. 6, pp. 3399–3408, Jun. 2015.
[21] H. Nian and W. Hu, "Torque ripple suppression method with reduced switching frequency for open-winding PMSM drives with common DC bus," *IEEE Trans. Ind. Electron.*, vol. 66, no. 1, pp. 674–684, Jan. 2018.
[22] Z. Shen *et al.*, "A novel zero-sequence current elimination PWM scheme for an open-winding PMSM with common DC bus," *IEEE Trans. Power Electron.*, vol. 34, no. 12, pp. 12476–12490, Dec. 2019.
[23] W. Wang *et al.*, "New three-phase current reconstruction for PMSM drive with hybrid space vector pulsewidth modulation technique," *IEEE Trans. Power Electron.*, vol. 36, no. 1, pp. 662–673, Jan. 2021.
[24] J. Lu, Y. Hu, J. Liu, and H. Wen, "Self-calibration of phase current sensors with sampling errors by multipoint sampling of current values in a single PWM cycle," *IEEE Trans. Ind. Electron.*, vol. 68, no. 4, pp. 2942–2951, Apr. 2021.
[25] J. Lu, X. Zhang, Y. Hu, J. Liu, C. Gan, and Z. Wang, "Independent phase current reconstruction strategy for IPMSM sensorless control without using null switching states," *IEEE Trans. Ind. Electron.*, vol. 65, no. 6, pp. 4492–4502, Jun. 2018.
[26] G. Wang *et al.*, "Current reconstruction considering time-sharing sampling errors for single DC-link shunt motor drives," *IEEE Trans. Power Electron.*, vol. 36, no. 5, pp. 5760–5770, May 2021.
[27] J. Im and R. Kim, "Improved saliency-based position sensorless control of interior permanent-magnet synchronous machines with single DC-link current sensor using current prediction method," *IEEE Trans. Ind. Electron.*, vol. 65, no. 7, pp. 5335–5343, Jul. 2018.
[28] H. Yan, Y. Xu, W. Zhao, H. Zhang, and C. Gerada, "DC drift error mitigation method for three-phase current reconstruction with single hall current sensor," *IEEE Trans. Magn.*, vol. 55, no. 2, Feb. 2019, Art. no. 8100604.
[29] Y. Xu, H. Yan, J. Zou, B. Wang, and Y. Li, "Zero voltage vector sampling method for PMSM three-phase current reconstruction using single current sensor," *IEEE Trans. Power Electron.*, vol. 32, no. 5, pp. 3797–3807, May 2017.
[30] J. Ha, "Voltage injection method for three-phase current reconstruction in PWM inverters using a single sensor," *IEEE Trans. Power Electron.*, vol. 24, no. 3, pp. 767–775, Mar. 2009.
[31] H. Kim and T. M. Jahns, "Phase current reconstruction for AC motor drives using a DC link single current sensor and measurement voltage vectors," *IEEE Trans. Power Electron.*, vol. 21, no. 5, pp. 1413–1419, Sep. 2006.
[32] J. Lu, Y. Hu, J. Liu, and Z. Wang, "All current sensor survivable IPMSM drive with reconfigurable inverter," *IEEE Trans. Ind. Electron.,* vol. 67, no. 8, pp. 6331–6341, Aug. 2020.
[33] Y. Cho, T. LaBella, and J.-S. Lai, "A three-phase current reconstruction strategy with online current offset compensation using a single current sensor," *IEEE Trans. Ind. Electron.*, vol. 59, no. 7, pp. 2924–2933, Jul. 2012.
[34] H. Yan, Y. Xu, J. Zou, Y. Fang, and F. Cai, "A novel open-circuit fault diagnosis method for voltage source inverters with a single current sensor," *IEEE Trans. Power Electron.*, vol. 33, no. 10, pp. 8775–8786, Oct. 2018.
[35] F. Blaabjerg, J. K. Pedersen, U. Jaeger, and P. Thoegersen, "Single current sensor technique in the DC link of three-phase PWM-VSI inverters: A review and a novel solution," *IEEE Trans. Ind. Appl.*, vol. 33, no. 5, pp. 1241–1253, Sep./Oct. 1997.
[36] Y. Cho, A. Koran, H. Miwa, B. York, and J. S. Lai, "An active current reconstruction and balancing strategy with DC-link current sensing for a multi-phase coupled-inductor converter," *IEEE Trans. Power Electron.*, vol. 27, no. 4, pp. 1697–1705, Apr. 2012.
[37] Y. S. Lai, Y. K. Lin, and C. W. Chen, "New hybrid pulsewidth modulation technique to reduce current distortion and extend current reconstruction range for a three-phase inverter using only DC-link sensor," *IEEE Trans. Power Electron.*, vol. 28, no. 3, pp. 1331–1337, Mar. 2013.
[38] V. Verma, C. Chakraborty, S. Maiti, and Y. Hori, "Speed sensorless vector controlled induction motor drive using single current sensor," *IEEE Trans. Energy Convers.*, vol. 28, no. 4, pp. 938–950, Dec. 2013.
[39] C. Chakraborty and V. Verma, "Speed and current sensor fault detection and isolation technique for induction motor drive using axes transformation," *IEEE Trans. Ind. Electron.*, vol. 62, no. 3, pp. 1943–1954, Mar. 2015.
[40] S. Ichikawa, M. Tomita, S. Doki, and S. Okuma, "Sensorless control of synchronous reluctance motors based on extended EMF models considering magnetic saturation with online parameter identification," *IEEE Trans. Ind. Appl.*, vol. 42, no. 5, pp. 1264–1274, Sep. 2006.
[41] Z. Mynar, P. Vaclavek, and P. Blaha, "Synchronous reluctance motor parameter and state estimation using extended kalman filter and current derivative measurement," *IEEE Trans. Ind. Electron.*, vol. 68, no. 3, pp. 1972–1981, Mar. 2021.
[42] D. Wang, K. Lu, and P. O. Rasmussen, "Improved closed-loop flux observer based sensorless control against system oscillation for synchronous reluctance machine drives," *IEEE Trans. Power Electron.*, vol. 34, no. 5, pp. 4593–4602, May 2019.

Chong Zhang was born in Hubei, China, in 1998. He received the B.S. degree in electrical engineering in 2020 from the Huazhong University of Science and Technology, Wuhan, China, where he is currently working toward the Ph.D. degree with the School of Electrical and Electronic Engineering, Huazhong University of Science and Technology, Wuhan, China.

His research interests include the driving topology and control strategy of permanent magnet machines and synchronous reluctance machines.

Chun Gan (Member, IEEE) received the B.S. and M.S. degrees in electrical engineering from the China University of Mining and Technology, Jiangsu, China, in 2009 and 2012, respectively, and the Ph.D. degree in electrical engineering and motor drives from Zhejiang University, Hangzhou, China, in 2016.

He is currently a Professor with the School of Electrical and Electronic Engineering, Huazhong University of Science and Technology, Wuhan, China. From 2016 to 2018, he was a Research Associate with the Department of Electrical Engineering and Computer Science, University of Tennessee, Knoxville, TN, USA. He has authored or coauthored more than 80 peer-reviewed technical papers, including more than 50 IEEE transaction papers, and has more than 20 issued/published invention patents. His research interests include electric motor drives, electric motor converters, motor design, electric vehicles, electrified transportation, and high-efficiency power converters.

Dr. Gan was the recipient of the 2018 Highlighted Paper Award from the IEEE TRANSACTIONS ON POWER ELECTRONICS, the 2018 Marie Sklodowska-Curie Actions Seal of Excellence Award from European Commission, and the 2019 Best Paper Award from ICEMS.

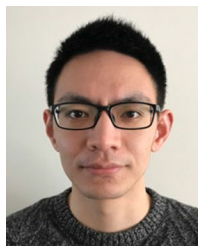

Kai Ni (Member, IEEE) was born in Jiangsu, China. He received the B.Eng.(Hons.) and Ph.D. degrees in electrical engineering from the University of Liverpool, Liverpool, U.K., in 2016 and 2019, respectively.

After obtaining the support from the Postdoctoral International Exchange Program, in December 2019, he joined the School of Electrical and Electronic Engineering, Huazhong University of Science and Technology, in 2019, as a Postdoctoral Researcher. His research interests include modeling, control and stability analysis of doubly fed induction machines, power electronic converters, and aircraft/shipboard power systems.

Dr. Ni was the recipient of the 2019 Chinese Government Award for Outstanding Self-Financed Students Abroad.

Zhiyue Yu (Student Member, IEEE) was born in Shandong, China, in 1996. He received the B.S. degree in electrical engineering and automation from Chongqing University, Chongqing, China, in 2018, and the M.S. degree in electrical engineering in 2021 from the Huazhong University of Science and Technology, Wuhan, China, where he is currently working toward the Ph.D. degree with the School of Electrical and Electronic Engineering.

His research interests include the driving topology and control strategy of permanent magnet machines and reluctance machines.

Haochen Shi (Member, IEEE) received the B.S. degree from China Three Gorge University, Yichang, China, in 2014, the M.Eng. degree from the University of Leicester, Leicester, U.K., in 2015, and the Ph.D. degree from the University of Liverpool, Liverpool, U.K, in 2020, all in electrical engineering.

He is currently a Postdoctoral Fellow with the Huazhong University of Science and Technology, Wuhan, China. His current research interests include bidirectional dc–dc converter, electrical vehicles, wireless power transfer, and renewable power conversion systems.

Ronghai Qu (Fellow, IEEE) was born in China. He received the B.E.E. and M.S.E.E. degrees from Tsinghua University, Beijing, China, in 1993 and 1996, respectively, and the Ph.D. degree from the University of Wisconsin—Madison, Madison, WI, USA, in 2002, all in electrical engineering.

In 1998, he joined Wisconsin Electric Machines and Power Electronics Consortiums, University of Wisconsin–Madison, as a Research Assistant. He became a Senior Electrical Engineer with Northland, a Scott Fetzer Company, Westlake, OH, USA, in 2002. Since 2003, he has been with General Electric (GE) Global Research Center, Niskayuna, NY, USA, as a Senior Electrical Engineer with Electrical Machines and Drives Laboratory. Since 2010, he has been a Professor with the Huazhong University of Science and Technology, Wuhan, China. He has authored more than 50 published technical papers and is the holder of more than 40 patents or patent applications.

Prof. Qu is a Full Member of Sigma Xi. He was the recipient of several awards from GE Global Research Center from 2003, including the Technical Achievement and Management Awards, and the 2003 and 2005 Best Paper Awards, Third Prize, from the Electric Machines Committee of the IEEE Industry Applications Society in 2002 and 2004 IAS Annual Meeting, respectively.